ELSEVIER

European Journal of Mechanics B/Fluids 21 (2002) 413–427

EUROPEAN JOURNAL OF MECHANICS B/FLUIDS

Direct numerical simulation of the turbulent flow in a pipe with annular cross section

Maurizio Quadrio [a,*], Paolo Luchini [b]

[a] *Dipartimento di Ingegneria Aerospaziale Politecnico di Milano, Italy*
[b] *Dipartimento di Ingegneria Meccanica Università di Salerno, Italy*

Received 12 January 2002; received in revised form 23 April 2002; accepted 25 April 2002

Abstract

The turbulent flow in a pipe of annular cross section is studied for the first time through a direct numerical simulation (DNS) using the Navier–Stokes equations written in cylindrical coordinates. To this aim a novel numerical method is developed, which extends to the cylindrical coordinate system an existing, efficient method designed for cartesian coordinates, and allows us to eliminate the pressure and formulate the problem in two scalar unknowns. The unnecessary increase of resolution at smaller radius typically brought about by polar coordinates, with its consequent stability limitations, is avoided by changing the number of azimuthal Fourier modes with the radial coordinate itself. In addition, the azimuthal extension of the computational domain is reduced, for the cases with lowest curvature, by considering only a part of the annulus, without loss of physical significance of the results. A computer code based on this method is run on a desktop PC for the simulation (with up to 16 million degrees of freedom) of the turbulent flow in a pipe with annular cross section, in a range of relatively low curvatures. This investigation highlights that curvature effects are already evident, even on first order turbulence statistics like the mean axial velocity distribution, in a low-curvature range where it is commonly believed that the flow should be hardly distinguishable from the flow over a plane surface.

Keywords: Navier–Stokes equations; Cylindrical coordinates; Spectral methods; Turbulence; Annular pipe flow

1. Introduction

Amongst the most important turbulent wall flows that can be studied through direct numerical simulation (DNS), one can mention turbulent plane-channel flows and boundary layers on one side, and turbulent flows in pipes and ducts with annular cross sections on the other. The former naturally call for the use of a cartesian coordinate system, whereas the Navier–Stokes equations written in cylindrical coordinates are well suited for the numerical simulation of the latter.

A large number of numerical studies exist, concerning elementary flows based on the Navier–Stokes equations in cartesian coordinates. Flows which can be easily described in cylindrical coordinates are by no means less interesting; beside pipe flow, annular-duct flows play a role in important engineering applications like axial, coaxial and annular jets with and without swirl, and flow in wells being drilled [1]. They bear, moreover, speculative interest, since the effects of the transverse curvature, although not so severe as those of streamwise curvature, can significantly impact the mean flow and the low-order turbulence statistics, as shown for example in [2]. Such flows are nonetheless little studied through DNS.

There are many open issues concerning the effects of transverse curvature on turbulent wall flow. In comparison with the planar case, in such flow the picture is complicated by the presence of an additional characteristic length, the radius of curvature of the wall. Two length scales generally stand out in turbulent wall flow: one is the viscous length scale ν/u_τ, where ν is

* Corresponding author. Address: Dipartimento di Ingegneria Aerospaziale del Politecnico di Milano, via La Masa 34, 20158 Milano, Italy.
E-mail addresses: maurizio.quadrio@polimi.it (M. Quadrio), luchini@unisa.it (P. Luchini).

0997-7546/02/$ – see front matter
PII: S0997-7546(02)01192-5

the viscosity of the fluid and u_τ is the friction velocity; the other is an external length scale, for example the boundary layer thickness or, in the case of a pipe with annular cross section, the annular gap. Dimensional analysis suggests that the effects of the radius of transverse curvature $\mathcal{R}$ of the wall can be expressed through one of the following two nondimensional groups: the radius of curvature $\mathcal{R}^+ = \mathcal{R}u_\tau/\nu$ in inner units, or the ratio $\mathcal{R}/\delta$, where δ is an external length scale. It is believed [2,3] that the effects of transverse curvature become noticeable on the low order statistical moments of the turbulent velocity fluctuations only when the external curvature parameter $\gamma = \delta/\mathcal{R}$ is greater than unity. In this high-curvature regime, the perhaps most prominent effect is an increase in the friction factor, together with a dependency of the mean velocity profile on curvature, on which no definite consensus exists yet in the literature: some authors [4] indeed propose a curvature correction in the viscous sublayer, while others [3] surmise a dependency of the log-law on γ, and others [5] also include a dependency on $\mathcal{R}^+$. At least part of this uncertainty can be ascribed to experimental problems, particularly to difficulties in obtaining an exactly axisymmetric stable setup and in accurately measuring or estimating the friction velocity. Owing to its experimental and numerical complexity, the low-curvature regime is still largely unexplored, and there is no clear consensus to date as to when transverse curvature of the wall begins to affect the low-order turbulence statistics.

From a numerical viewpoint, to our best knowledge, the turbulent flow between two concentric cylinders has been studied through fully resolved DNS in only one paper, namely the one by Neves et al. [2]. They employed a spectral numerical method and studied the effect of transverse curvature on the turbulence statistics computed over the inner, transversely convex wall only. Their objective was, in fact, to study the cylindrically symmetrical turbulent boundary layer which grows spatially over very thin and long rods: therefore the annular geometry was used rather as an approximation of an unbounded outer space than on its own account, and a zero-stress boundary condition was imposed at the surface of the outer cylinder. Moreover, as recognized by the authors themselves, in proximity of the outer cylinder there was definitely inadequate spatial resolution, and indeed in [2] the outer boundary is not given any consideration at all. In addition, the curvature parameter γ was substantially higher than the values considered in the present paper, so that a completely different region of parameter space is now investigated.

Satake and Kawamura [6] addressed the turbulent flow in an annular pipe through Large Eddy Simulation, at a higher Reynolds number than [2] and at a similarly large γ, but in an actual annular duct, i.e., with no-slip conditions imposed on both walls. Kawamura [private communication] also tried to perform a DNS study of the same flow at a lower Reynolds number, but encountered severe numerical problems. An annular geometry similar to those considered in the present paper was used by Shapiro et al. [7] for the purpose of studying linear and nonlinear stability of a laminar flow with the aid of a DNS finite-volume code. An extension to the fully turbulent regime was not attempted, as the required computational resources were reportedly too high. Hence a DNS of a turbulent flow in an annular pipe has yet to be performed.

The fact that, despite its practical relevance, turbulent flow in pipes and annular ducts has not been so deeply studied through DNS as its planar counterpart, can be at least partially ascribed to the peculiar numerical difficulties associated with the cylindrical coordinate system. For the cartesian coordinate system, a very effective formulation of the equations of motion was presented in [8], the pioneering and widely-referenced paper on the DNS of turbulent plane channel flow. This formulation has since been employed in many of the DNSs of turbulent wall flow in planar geometries. It basically consists in the substitution of the continuity and momentum equations written in primitive variables with two scalar equations, one (second-order) for the wall-normal component of vorticity and one (fourth-order) for the wall-normal component of velocity. This procedure is appealing, since pressure is eliminated from the equations, and the reconstruction of the other two velocity components is immediate when a Fourier expansion is adopted for the homogeneous directions. A very high computational efficiency can thus be achieved.

An extension of this formulation to the cylindrical case was until now missing. Most of the existing numerical studies of turbulent flow in cylindrical coordinates write the governing equations in primitive variables, and use each a different numerical method, ranging from simple finite-difference schemes (e.g., [9]) to finite volumes [7], to complex spectral multi-domain techniques (as in [10,11]), but most often remain inside the pressure-correction approach. The paper [2] is based on a spectral discretization, but the calculation of pressure is still needed for the numerical solution of the equations.

Beside the problem of possible singularities on the axis (which is of no concern when dealing with an annular geometry), an additional, severe, difficulty entailed by cylindrical coordinates is the dependence of azimuthal resolution of the computational grid on the radial coordinate. A sufficiently high spatial resolution of DNS calculations is known to be crucial for the reliability of the computed turbulence statistics, especially in the near-wall region. On the other hand, an excessive resolution lowers the stability limit of an explicit or partially explicit time-advancement scheme. The azimuthal resolution, when set so as to be sufficient near the outer wall of an annular pipe, becomes unnecessarily high when the inner wall is approached. If, on the other hand, the inner wall is chosen to dictate the spatial resolution, the turbulent scales are gradually less and less well resolved in the azimuthal direction when the distance from the inner wall increases. In addition, if one wants to consider low curvatures, the wide azimuthal extension of the annulus determines a tremendous expense of computational resources.

In this paper we present an extension of the efficient cartesian method for the DNS of turbulent wall flows to the cylindrical geometry. This extension allows us to maintain the very same structure of a numerical code developed for the plane channel flow, with a very modest increase of computational cost for the same number of degrees of freedom. Moreover, a strategy to

avoid the unnecessary clustering of azimuthal resolution near the inner wall and the increase of computing cost with decreasing curvature is described. This numerical method is then used to study the effects of mild transverse curvature on the statistics of the turbulent flow in an annular pipe, with the aim of highlighting the differences with planar flow at low curvature values.

The outline of the paper is as follows. In the next section the reduction of the Navier–Stokes system to two scalar equations will be worked out in cylindrical coordinates. In Section 3 the numerical method will be described, together with the solution adopted to keep the azimuthal resolution under control. Section 4 will be devoted to the illustration of the parameters defining our computational experiments: in particular, two values of the curvature parameter γ will be considered. In Sections 5 and 6 the results will be described in terms of the mean flow properties and the main turbulence statistics. Finally, in Section 7 some conclusions will be drawn.

2. Governing equations

The coordinate system used in the present paper is illustrated in Fig. 1, where a sketch of the annular duct is shown: x, r and θ denote the axial, radial and azimuthal coordinates, and u, v and w the corresponding components of the velocity vector. The inner cylinder has radius $\mathcal{R}_i$ and the outer cylinder has radius $\mathcal{R}_o$. The reference length δ is taken to be one half of the gap width:

$$\delta = \frac{\mathcal{R}_o - \mathcal{R}_i}{2}.$$

The reference velocity is chosen to be the bulk velocity U_b, so that a bulk Reynolds number can be defined as:

$$\mathrm{Re}_b = \frac{U_b 2\delta}{\nu},$$

where ν is the kinematic viscosity of the fluid. These definitions are such that the usual Reynolds number of a plane duct is recovered in the limit of zero curvature.

The non-dimensional Navier–Stokes equations for an incompressible fluid are, in cylindrical coordinates:

$$\frac{\partial u}{\partial x} + \frac{1}{r}\frac{\partial (r v)}{\partial r} + \frac{1}{r}\frac{\partial w}{\partial \theta} = 0, \tag{1}$$

$$\frac{\partial u}{\partial t} + u\frac{\partial u}{\partial x} + v\frac{\partial u}{\partial r} + \frac{w}{r}\frac{\partial u}{\partial \theta} = -\frac{\partial p}{\partial x} + \frac{1}{\mathrm{Re}}\nabla^2 u, \tag{2a}$$

$$\frac{\partial v}{\partial t} + u\frac{\partial v}{\partial x} + v\frac{\partial v}{\partial r} + \frac{w}{r}\frac{\partial v}{\partial \theta} - \frac{w^2}{r} = -\frac{\partial p}{\partial r} + \frac{1}{\mathrm{Re}}\left(\nabla^2 v - \frac{v}{r^2} - \frac{2}{r^2}\frac{\partial w}{\partial \theta}\right), \tag{2b}$$

$$\frac{\partial w}{\partial t} + u\frac{\partial w}{\partial x} + v\frac{\partial w}{\partial r} + \frac{w}{r}\frac{\partial w}{\partial \theta} + \frac{vw}{r} = -\frac{1}{r}\frac{\partial p}{\partial \theta} + \frac{1}{\mathrm{Re}}\left(\nabla^2 w - \frac{w}{r^2} + \frac{2}{r^2}\frac{\partial v}{\partial \theta}\right), \tag{2c}$$

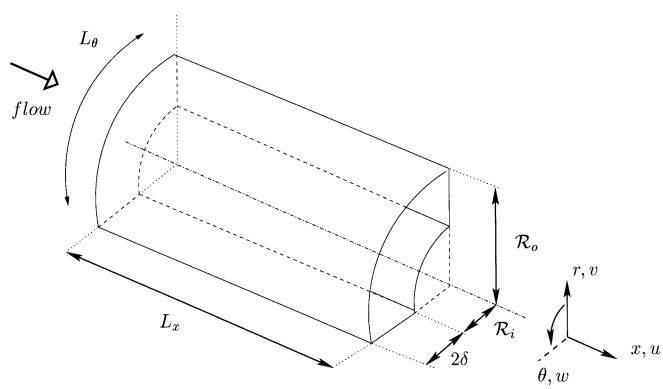

Fig. 1. Sketch of the computational domain and the coordinate system used in the present work.

where the (scalar) Laplacian operator ∇^2 takes the form:

$$\nabla^2 = \frac{\partial^2}{\partial x^2} + \frac{1}{r}\frac{\partial}{\partial r}\left(r\frac{\partial}{\partial r}\right) + \frac{1}{r^2}\frac{\partial^2}{\partial \theta^2}. \tag{3}$$

As the flow will be assumed to be periodic in the axial and azimuthal directions, all variables can be conveniently represented as Fourier series along the x and θ coordinates. The symbols α and m will respectively denote the axial and azimuthal wavenumber. On defining $k^2 = (m/r)^2 + \alpha^2$, and introducing the Chandrasekhar notation:

$$D(f) = \frac{\partial f}{\partial r}, \qquad D_*(f) = \frac{\partial f}{\partial r} + \frac{f}{r},$$

the Fourier-transformed Laplacian operator (3) can be written in the compact form:

$$\nabla^2 = -k^2 + D_* D.$$

The transformed equations, where a hat indicates the Fourier component of the corresponding variable, are:

$$\mathrm{i}\alpha\widehat{u} + D_*(\widehat{v}) + \frac{\mathrm{i}m}{r}\widehat{w} = 0, \tag{4}$$

$$\frac{\partial \widehat{u}}{\partial t} = -\mathrm{i}\alpha\hat{p} + \frac{1}{\mathrm{Re}}\left(D_* D(\widehat{u}) - k^2\widehat{u}\right) + H_{\widehat{u}}, \tag{5a}$$

$$\frac{\partial \widehat{v}}{\partial t} = -D(\hat{p}) + \frac{1}{\mathrm{Re}}\left(D D_*(\widehat{v}) - k^2\widehat{v} - \frac{2\mathrm{i}m}{r^2}\widehat{w}\right) + H_{\widehat{v}}, \tag{5b}$$

$$\frac{\partial \widehat{w}}{\partial t} = -\frac{\mathrm{i}m}{r}\hat{p} + \frac{1}{\mathrm{Re}}\left(D D_*(\widehat{w}) - k^2\widehat{w} + \frac{2\mathrm{i}m}{r^2}\widehat{v}\right) + H_{\widehat{w}}. \tag{5c}$$

In these expressions, the nonlinear convective terms have been grouped under the following definitions:

$$H_{\widehat{u}} = -\mathrm{i}\alpha\widehat{uu} - D_*(\widehat{uv}) - \frac{\mathrm{i}m}{r}\widehat{uw}, \tag{6a}$$

$$H_{\widehat{v}} = -\mathrm{i}\alpha\widehat{uv} - D_*(\widehat{vv}) - \frac{\mathrm{i}m}{r}\widehat{vw} + \frac{1}{r}\widehat{ww}, \tag{6b}$$

$$H_{\widehat{w}} = -\mathrm{i}\alpha\widehat{uw} - D(\widehat{vw}) - \frac{\mathrm{i}m}{r}\widehat{ww} - \frac{2}{r}\widehat{vw}, \tag{6c}$$

where for example $\widehat{uv}$ indicates the Fourier transform of the product uv of two velocity components.

2.1. A second-order scalar equation for the radial vorticity

The radial component η of the vorticity vector, in Fourier space, is given by

$$\hat{\eta} = \frac{\mathrm{i}m}{r}\widehat{u} - \mathrm{i}\alpha\widehat{w}.$$

Following a similar procedure as in the cartesian case, an equation for $\hat{\eta}$, which does not involve pressure, can be written by taking the radial component of the curl of the momentum equation:

$$\frac{\mathrm{i}m}{r}\frac{\partial \widehat{u}}{\partial t} - \mathrm{i}\alpha\frac{\partial w}{\partial t} = \frac{1}{\mathrm{Re}}\left[\frac{\mathrm{i}m}{r}D_* D(\widehat{u}) - \mathrm{i}\alpha D D_*(\widehat{w}) - k^2\left(\frac{\mathrm{i}m}{r}\widehat{u} - \mathrm{i}\alpha\widehat{w}\right) + 2\frac{m\alpha}{r^2}\widehat{v}\right] + \frac{\mathrm{i}m}{r}H_{\widehat{u}} - \mathrm{i}\alpha H_{\widehat{w}}. \tag{7}$$

On remembering the definition of the operators D and D_*, and the fact that:

$$D D_* = D_* D - \frac{1}{r^2}$$

one can substitute $(\mathrm{i}m/r)\widehat{u} - \hat{\eta}$ for $\mathrm{i}\alpha\widehat{w}$ in the preceding equation, and write the following second-order equation for $\hat{\eta}$:

$$\frac{\partial \hat{\eta}}{\partial t} = \frac{1}{\mathrm{Re}}\left(D D_*(\hat{\eta}) - k^2\hat{\eta} + 2\frac{\mathrm{i}m}{r^2}D(\widehat{u}) + 2\frac{m\alpha}{r^2}\widehat{v}\right) + \frac{\mathrm{i}m}{r}H_{\widehat{u}} - \mathrm{i}\alpha H_{\widehat{w}}. \tag{8}$$

Eq. (8) must be solved with the two boundary conditions $\hat{\eta} = 0$ at $r = \mathcal{R}_i$ and $\hat{\eta} = 0$ at $r = \mathcal{R}_o$, and a suitable initial condition in time. The equation has an overall structure which is analogous to that of the corresponding equation in the cartesian case, except for some remaining curvature terms which contain $\widehat{v}$ and the first radial derivative of $\widehat{u}$.

2.2. A fourth-order scalar equation for the radial velocity

The derivation of a pressure-free equation for the radial component $\widehat{v}$ of the velocity is less straightforward but possible, provided repeated use is made of the continuity equation in order to obtain the necessary simplifications.

The first step consists in taking the time derivative of the Fourier-transformed continuity Eq. (4), which can be written as

$$\frac{\partial D_*(\widehat{v})}{\partial t} = -\mathrm{i}\alpha\frac{\partial \widehat{u}}{\partial t} - \frac{\mathrm{i}m}{r}\frac{\partial \widehat{w}}{\partial t}.$$

Here the time derivatives of $\widehat{u}$ and $\widehat{w}$ can be replaced by the corresponding expressions extracted from Eqs. (5a) and (5c), thus giving:

$$\frac{\partial D_*(\widehat{v})}{\partial t} = -k^2\hat{p} - \mathrm{i}\alpha\left[\frac{1}{\mathrm{Re}}\left(D_*D(\widehat{u}) - k^2\widehat{u}\right) + H_{\widehat{u}}\right] - \frac{\mathrm{i}m}{r}\left[\frac{1}{\mathrm{Re}}\left(DD_*(\widehat{w}) - k^2\widehat{w} + 2\frac{\mathrm{i}m}{r^2}\widehat{v}\right) + H_{\widehat{w}}\right].$$

The continuity equation can be invoked again to simplify some terms, together with the relations obtained by applying the operators D/r and D^2 to it, namely:

$$-\frac{1}{r}DD_*(\widehat{v}) = \frac{\mathrm{i}\alpha}{r}D(\widehat{u}) + \frac{\mathrm{i}m}{r^2}D(\widehat{w}) - \frac{\mathrm{i}m}{r^3}\widehat{w},$$
$$-D^2D_*(\widehat{v}) = \mathrm{i}\alpha D^2(\widehat{u}) + \frac{\mathrm{i}m}{r}D^2(\widehat{w}) + 2\frac{\mathrm{i}m}{r^3}\widehat{w} - 2\frac{\mathrm{i}m}{r^2}D(\widehat{w}).$$

By also applying the relation

$$D_*DD_*(\widehat{v}) = D^2D_*(\widehat{v}) + \frac{1}{r}DD_*(\widehat{v}),$$

after some algebra, the following expression for $\hat{p}$ is obtained:

$$\hat{p} = -\frac{1}{\mathrm{Re}}\frac{1}{k^2}\left[k^2D_*(\widehat{v}) - D_*DD_*(\widehat{v}) - 2\frac{m^2}{r^3}\widehat{v} + 2\frac{\mathrm{i}m}{r^2}D(\widehat{w}) - 2\frac{\mathrm{i}m}{r^3}\widehat{w}\right] - \frac{1}{k^2}\left[\frac{\partial D_*(\widehat{v})}{\partial t} + \mathrm{i}\alpha H_{\widehat{u}} + \frac{\mathrm{i}m}{r}H_{\widehat{w}}\right].$$

This expression can be differentiated with respect to the radial coordinate, and then substituted into Eq. (5b) to get rid of $\hat{p}$ altogether. Eventually the fourth-order equation for $\widehat{v}$ emerges in the final form:

$$\begin{aligned}\frac{\partial}{\partial t}\left[\widehat{v} - D\left(\frac{1}{k^2}D_*(\widehat{v})\right)\right] = {} & \frac{1}{\mathrm{Re}}D\left\{\frac{1}{k^2}\left[k^2D_*(\widehat{v}) - D_*DD_*(\widehat{v}) - 2\frac{m^2}{r^3}\widehat{v} + 2\frac{\mathrm{i}m}{r^2}D(\widehat{w}) - 2\frac{\mathrm{i}m}{r^3}\widehat{w}\right]\right\} \\ & + \frac{1}{\mathrm{Re}}\left(-k^2\widehat{v} + DD_*(\widehat{v}) - 2\frac{\mathrm{i}m}{r^2}\widehat{w}\right) + D\left[\frac{1}{k^2}\left(\mathrm{i}\alpha H_{\widehat{u}} + \frac{\mathrm{i}m}{r}H_{\widehat{w}}\right)\right] + H_{\widehat{v}}. \qquad (9)\end{aligned}$$

Eq. (9) must be solved with the four boundary conditions $\widehat{v} = 0$ and $\partial\widehat{v}/\partial r = 0$ at $r = \mathcal{R}_i$ and $r = \mathcal{R}_o$, and a suitable initial condition in time. It is very similar in structure to the corresponding equation for the cartesian case, except that curvature terms proportional to $\widehat{w}$ and to its radial derivative are present.

3. The numerical method

Thanks to the periodic boundary conditions, all the flow variables have been discretized as finite sums of Fourier modes, or truncated Fourier series, in the axial and azimuthal directions. For example, the radial component v of the velocity vector is represented as:

$$v(x,\theta,r,t) = \sum_{h=-N_x}^{+N_x}\sum_{l=-N_\theta(r)}^{+N_\theta(r)}\widehat{v}_{hl}(r,t)\mathrm{e}^{\mathrm{i}\alpha x}\mathrm{e}^{\mathrm{i}m\theta},$$

where

$$\alpha = \frac{2\pi h}{L_x} = \alpha_0 h, \qquad m = \frac{2\pi l}{L_\theta} = m_0 l.$$

Here h and l are integer indices corresponding to the axial and azimuthal direction respectively, and α_0 and m_0 are the fundamental wavenumbers in each of these directions, defined in terms of the axial length L_x of the computational domain and its azimuthal extension L_θ expressed in radians.

However, in a cylindrical coordinate system, the actual azimuthal size of the computational domain decreases with r; if the required spatial resolution, or number of Fourier modes, is set up based on the most demanding region of the flow field, i.e., the outer wall, then the spatial resolution becomes unnecessarily high when the inner wall is approached. This not only implies a waste of computational resources, but might also induce numerical stability problems.

To overcome this difficulty, we have made the truncation of the azimuthal Fourier series a function of the radial position. Key to our procedure is that, whereas in a collocation approach changing the resolution with radius would have involved multiple interpolations and numerical diffusion, in a spectral representation dropping a few Fourier modes at the high end of the spectrum is a smooth operation, which does not introduce any spatially localized error.

Given this intrinsic smoothness of the Fourier series, we are free to make the number N_θ of azimuthal Fourier modes an arbitrary function $N_\theta(r)$ of the radial coordinate. The simplest and most natural choice is a linear function $N_\theta(r)$, from a maximum value $N_{\theta,\max}$ at $r = \mathcal{R}_o$ down to a minimum $N_{\theta,\min}$ at $r = \mathcal{R}_i$, with $N_{\theta,\min}$ and $N_{\theta,\max}$ proportional to the inner and outer radii themselves so as to keep the *same* effective spatial resolution throughout the whole domain. This is equivalent to assuming that the Fourier modes $\widehat{v}_{hl}$ with $|l| \leqslant N_{\theta,\min}$ are defined in the whole annular gap, i.e., for $\mathcal{R}_i \leqslant r \leqslant \mathcal{R}_o$, while any mode $\widehat{v}_{hl}$ with $N_{\theta,\min} < |l| \leqslant N_{\theta,\max}$ only exists for $\bar{r}(l) < r < \mathcal{R}_o$, where $\bar{r}(l)$ is a suitable radial position, function of the index l, intermediate between the two walls. These modes are assumed to become zero at the lower end of this interval, just as all modes beyond $N_{\theta,\max}$ implicitly are everywhere, and the necessary boundary conditions for their governing radial differential equation are thus provided.

From the point of view of computer programming, a comb array of Fourier coefficients whose number varies with l (and possibly h too, even if this feature is not presently used) has been implemented through a suitable memory management, where a two-dimensional array of pointers is used to reference variable-sized one-dimensional arrays, each of which stores all and only the nonzero coefficients in a radial line, from $r = \mathcal{R}_o$ down to $\bar{r}(l)$. This procedure, some more details of which can be found in [12], is able to reduce the computational cost of DNS in cylindrical geometry, thanks to the reduction in the number of active Fourier modes, and at the same time to avoid the numerical stability problems which could otherwise derive from an overfine resolution of the innermost region.

The radial discretization of Eqs. (8) and (9) is performed through finite differences over a computational molecule composed of five unevenly spaced points. The use of finite differences for the DNS of turbulent flows is a recognized reliable discretization method (see, for example, [13]), allowing flexibility in the boundary conditions, and relative ease of programming. It also has additional advantages in minimizing communication requirements when the numerical code is to be ported to parallel architectures. By using a computational molecule composed of five grid points most of the radial differencing operators can be constructed at fourth-order accuracy, while the operator DD_*DD_* is discretized with second-order accuracy only. The overall scheme is therefore asymptotically second-order accurate when the radial step size tends to zero; the accuracy of the code at practical values of the step size can nevertheless be expected to be comparable to that attainable with a fully fourth-order scheme, if it is noticed that the term DD_*DD_* only becomes significant near the walls, where the discretization error is reduced by the nonuniform step size anyway.

As far as the discretization in time is concerned, in the cartesian case time integration of the equations is usually performed by a partially implicit method, as classically described in [8]. A combination of an explicit (low-storage, third-order Runge–Kutta) scheme for the convective terms and an implicit (second-order Crank–Nicholson) scheme for the viscous terms is used here as well: the explicit part of the equations can benefit from a higher-accuracy scheme, while the stability-limiting part is subjected to an implicit advancement.

At first sight a difficulty exists in that the cylindrical equations (8) and (9) are coupled by curvature terms, and therefore a fully implicit treatment of the viscous terms would not allow each equation to be solved separately as in the cartesian case. To solve this difficulty, we just move the additional viscous curvature terms to the explicit part. In practice, we first solve Eq. (9) for $\widehat{v}$, with the $\widehat{w}$-dependent terms and all the H's as explicit terms, and then Eq. (8) for $\hat{\eta}$, with the terms containing $\widehat{v}$ and the first derivative of $\widehat{u}$ in the esplicit part. The algorithm is programmed so as to deal with a general evolutive differential equation written as

$$\frac{\partial unkn}{\partial t} = impl + expl,$$

where the unknown *unkn* is advanced in time with a method of choosable order, treating explicitly some terms grouped in *expl* and implicitly some others grouped in *impl*, and thus giving us the freedom to move terms from one group to the other and experiment with different combinations. The final choice was, for Eq. (9):

$$unkn = \widehat{v} - D\left(\frac{1}{k^2} D_*(\widehat{v})\right),$$

$$impl = \frac{1}{\mathrm{Re}}\left\{-k^2 v + 2DD_*(\widehat{v}) - D\left(\frac{1}{k^2} D_*DD_*(\widehat{v})\right) - D\left(\frac{2m^2}{k^2 r^3}\widehat{v}\right)\right\},$$

$$expl = \frac{1}{\mathrm{Re}}\left\{ D\left(\frac{2\mathrm{i}m}{k^2 r^2} D(\widehat{w}) - \frac{2\mathrm{i}m}{k^2 r^3}\widehat{w} \right) - 2\frac{\mathrm{i}m}{r^2}\widehat{w} \right\} + D\left[\frac{1}{k^2}\left(\mathrm{i}\alpha H_{\widehat{u}} + \frac{\mathrm{i}m}{r} H_{\widehat{w}} \right) \right] + H_{\widehat{v}},$$

and, for Eq. (8):

$$unkn = \hat{\eta}, \qquad impl = \frac{1}{\mathrm{Re}}\left(DD_*(\hat{\eta}) - k^2\hat{\eta} \right),$$

$$expl = \frac{1}{\mathrm{Re}}\left(\frac{2\mathrm{i}m}{r^2} D(\widehat{u}) + 2\frac{m\alpha}{r^2}\widehat{v} \right) + \frac{\mathrm{i}m}{r} H_{\widehat{u}} - \mathrm{i}\alpha H_{\widehat{w}}.$$

It can be envisaged that curvature terms, which contain low-order derivatives and are multiplied by inverse powers of r, can be treated explicitly without compromising the numerical stability of the time scheme. Our results fully support this view, and indeed we have been able to solve numerically the equations using a time step comparable with that used in the planar case, without incurring in any stability limitations.

Just as in the corresponding cartesian method, FFT algorithms are used during the explicit calculation of the nonlinear $H_{\widehat{u},\widehat{v},\widehat{w}}$ terms to compute the required convolutions in an efficient manner: the Fourier components of the velocity are transformed back into physical space, the nonlinear terms are evaluated by simple products and then retransformed into Fourier space. Dealiasing is performed by the 3/2 rule, expanding the number of collocation points before going from Fourier space to physical space so as to compute the convolutions exactly and avoid any spurious energy transfer from the high-frequency to the low-frequency modes. For the purpose of dealiasing, each plane of Fourier coefficients for a given radial position is moved in turn from the comb array to temporary storage before this operation; at the same time care is taken to change the size of the FFT so as to reflect the varying number of components present at each r.

After having solved, at each time step, the linear implicit parts of Eqs. (8) and (9) by direct band-matrix inversion, the remaining two velocity components, needed for the evaluation of the expressions (6a)–(6c) at later times, can be easily recovered, in Fourier space, from the definition of $\hat{\eta}$ and the continuity equation (4); namely:

$$\widehat{u}_{hl} = \frac{1}{k^2}\left(\mathrm{i}\alpha D_*(\widehat{v}_{hl}) - \frac{\mathrm{i}m}{r}\hat{\eta}_{hl} \right), \qquad \widehat{w}_{hl} = \frac{1}{k^2}\left(\mathrm{i}\alpha\hat{\eta}_{hl} + \frac{\mathrm{i}m}{r} D_*(\widehat{v}_{hl}) \right).$$

The singularity of this solution when $k^2 = 0$ reflects the fact that $\widehat{v}_{00}$ and $\hat{\eta}_{00}$ are identically zero. $\widehat{u}_{00}$ and $\widehat{w}_{00}$, on the other hand, are uncoupled at the implicit stage and obey, each, an equation similar to Eq. (8), which can be directly marched in time by a similar algorithm. At this stage the external forcing is imposed, either in the form of a pressure gradient or of a fixed flow rate. The simulations described in this paper are performed at fixed flow rate in the axial direction and zero mean pressure gradient in the azimuthal direction.

4. Computer code and computational parameters

The computer code for the numerical method described in the previous section has been obtained by modifying a previous cartesian version, which was in turn developed from scratch by us to implement a numerical method similar to the one described in [8], but using fourth-order accurate, compact finite differences in the wall-normal direction. The cartesian code (details of which are given in [12]) was written in a modular, compact and efficient form where different time and space discretizations and different choices of the implicit and explicit part can be easily interchanged without interfering with each other, and was thoroughly tested on its own right before proceeding with its extension to the cylindrical geometry. It was designed since the beginning with parallel computing in mind, and offers a very competitive speedup when run on a cluster of commodity computers with cheap communication interfaces. The cylindrical version shares with its cartesian counterpart a high computational efficiency in terms of both RAM requirements and CPU time: a full three-substeps Runge–Kutta time step for a cartesian case with 129 Fourier modes in both the homogeneous directions and 129 collocation points in the wall-normal direction takes only 50 CPU seconds on a single Pentium III 733 MHz CPU, and requires 96 MB of RAM.

As a preliminary step towards the full parallelization that is already implemented in the cartesian code, the present version of the cylindrical code can take advantage of 2-CPU SMP personal computers.

Two numerical experiments have been performed at the Reynolds number $\mathrm{Re}_b = 5600$, the same adopted in the reference planar case [8]. Two different cases have been considered, both in the mild-curvature regime: the first case has a geometry with $\mathcal{R}_i = 2\delta$ and $\mathcal{R}_o = 4\delta$, and the second case corresponds to $\mathcal{R}_i = \delta$ and $\mathcal{R}_o = 3\delta$. The curvature parameter, defined as $\gamma = \delta/\mathcal{R}_i$, is $\gamma = 0.5$ for the first case and $\gamma = 1$ for the second case. This definition is consistent with that adopted in [2], where the much higher values of $\gamma = 5$ and $\gamma = 11$ were studied.

As in [8], for both cases we have chosen $\alpha_0 = 0.5/\delta$, so that the period of the computational domain in the axial direction is $L_x = 4\pi\delta$ (which corresponds to $L_x^+ \sim 2260$). As far as the period in the circumferential direction is concerned, in the case

with $\gamma = 1$ a full turn has been considered, taking $m_0 = 1$: hence, the transversal length is $6\pi\delta$ at the outer wall and $2\pi\delta$ at the inner wall, as compared to $2\pi\delta$ of [8]. In the case of $\gamma = 0.5$, which is nearer to a planar flow, there is no need to consider a full turn; for it can be envisioned (and verified *a posteriori*) that the spanwise correlations go to zero much before that, and in particular at a distance comparable to the characteristic correlation distance of the planar case. This is particularly evident if the curvature is let tend to zero, where the planar case must be approached but the length of a full turn tends to infinity. We used here $m_0 = 2$, i.e., half a turn, corresponding to a transversal extension of $2\pi\delta$ (approximately 1130 wall units) at the inner wall. This is the spanwise length that was used by [8] and is generally accepted in the planar case; at the outer wall our domain is twice that length. As expected, an *a posteriori* examination of the autocorrelation functions (see, e.g., Fig. 7, right) confirms that they drop to zero for an azimuthal separation significantly less than half the extension of the computational domain. The use of $m_0 = 2$ was a key step to keep the required computational resources under control and make the investigation of the low-curvature regime possible.

The radial range is divided in 128 uneven intervals. For the case with $\gamma = 0.5$ 193 Fourier modes are considered for the longitudinal direction, with $-96 \leqslant \alpha/\alpha_0 \leqslant 96$, and 257 modes, with $-128 \leqslant m/m_0 \leqslant 128$, for the azimuthal direction at the outer wall, decreasing linearly to 129 at the inner wall. The case of $\gamma = 1$ has the same axial resolution, and 481 modes in the θ direction at $r = \mathcal{R}_o$, decreasing linearly to 161 at $r = \mathcal{R}_i$. This last case is the most computationally demanding, and is discretized in space with approximately 16 million degrees of freedom, defined as the number of unknown Fourier modes considered for $\hat{\eta}$ and $\widehat{v}$; the spatial resolution corresponds to $\Delta x^+ \sim 11.7$ and $\Delta z^+ \sim 7$; the radial step is $\Delta r^+ = 0.9{-}4.5$. Its numerical solution requires 410 MB of RAM, and every single flow field stored on disk for further analysis takes 136 MB of disk space. The computing time for this case is approximately 240s for a full Runge–Kutta time step, when an SMP personal computer (with two 500 MHz Intel CPUs) running the Linux operating system is used. The parallel efficiency with respect to the single-CPU version is around 190%.

The simulation at $\gamma = 0.5$ was started from a previously computed planar flow field, and the one at $\gamma = 1$ from a flow field of the preceding case. The flow fields have been adapted to the new discretization by spectral interpolation, and then the computer code has been run until any visible transient, shown by the time history of the mean friction at the inner and outer walls, disappeared. After that, the simulations have been run for further 100 δ/U_b units of time, in order to make sure that a statistically steady state is attained, independent of the initial conditions. Only then, during another 150 δ/U_b time units, flow fields have been stored on disk for the subsequent statistical analysis.

For both computational cases the time step has been set at $\Delta t = 0.02\ \delta/U_b$, comparable to the one employed in corresponding planar cases. In the final phase of the calculations, flow fields are stored on disk every 10 δ/U_b. At a later time these stored fields are used to compute the average statistics of interest, whereas the time history of the mean friction over the two walls and few other quantities are recorded at all times. Unless otherwise indicated, the mean quantities described in the following sections have been averaged over both time and the two homogeneous directions.

5. Mean flow properties

Table 1 shows the fundamental parameters of the computed mean flow for the two cases of $\gamma = 0.5$ and $\gamma = 1$, compared with the results for the planar case taken from [8] and the results at $\gamma = 5$ and $\gamma = 11$, relative to the inner wall only, from [2]. The friction coefficient over the inner wall increases with curvature, and the present simulations indicate that at $\gamma = 0.5$, where the inner radius is $\mathcal{R}_i^+ \sim 370$ expressed in wall units, the increase is about 7% compared to the planar case at a similar Reynolds number of $\mathrm{Re}_\tau = 180$. For the higher-curvature case with $\gamma = 1$, the increase in skin friction is about 14%, hence, seemingly

Table 1
Mean flow parameters for $\gamma = 0.5$ and $\gamma = 1$, compared with those reported in [8] for the plane channel flow and the DNS results of [2] relative to the higher-curvature regime

	$10^3 C_f$	Re_τ	Re_m	$U_b/u_{\tau,\mathrm{tot}}$	$U_{\max}/u_{\tau,\mathrm{tot}}$	$U_{\max}/U_b$
flat plate	6.04	≈ 180	≈ 3300	15.63	18.20	1.16
inner wall $\gamma = 0.5$	6.47	185.2	3273	15.55	18.18	1.169
inner wall $\gamma = 1$	6.87	190.7	3289	15.50	18.21	1.175
$\gamma = 5$ from [2]	8.07	214	3368			
$\gamma = 11$ from [2]	9.87	239	3418			
outer wall $\gamma = 0.5$	5.85	176.1	3273	15.55	18.18	1.169
outer wall $\gamma = 0.1$	5.76	174.6	3289	15.50	18.21	1.175

$u_{\tau,\mathrm{tot}}$ is the total friction velocity, i.e., the average of the two walls' friction velocities weighted by the corresponding wetted areas.

linear with the curvature parameter γ in the low-curvature regime. The friction coefficient over the outer wall presents an opposite behavior, but with a smaller relative decrease.

However, evaluating the total friction force which must be balanced by the pressure gradient to maintain the imposed flow rate, i.e., the average $c_{f,\mathrm{tot}}$ of the friction coefficients over the two walls weighted by the corresponding wetted areas, shows that the total friction is essentially unchanged from its planar value for both the curvatures considered.

The ratio between the bulk velocity and the friction velocity $u_{\tau,\mathrm{tot}}$ computed from the total friction coefficient $c_{f,\mathrm{tot}}$ decreases slightly with curvature, whereas the ratio between the maximum velocity $U_{\max}$ and $u_{\tau,\mathrm{tot}}$ does not exhibit significant variations. The ratio $U_{\max}/U_b$, on the other hand, increases slightly with curvature.

Fig. 2 (top) shows the computed profile, in the radial direction, of the mean axial velocity for $\gamma = 0.5$ and $\gamma = 1$. The laminar analytical solution corresponding to $\gamma = 1$ is also indicated in the figure, and presents a maximum of approximately 1.52

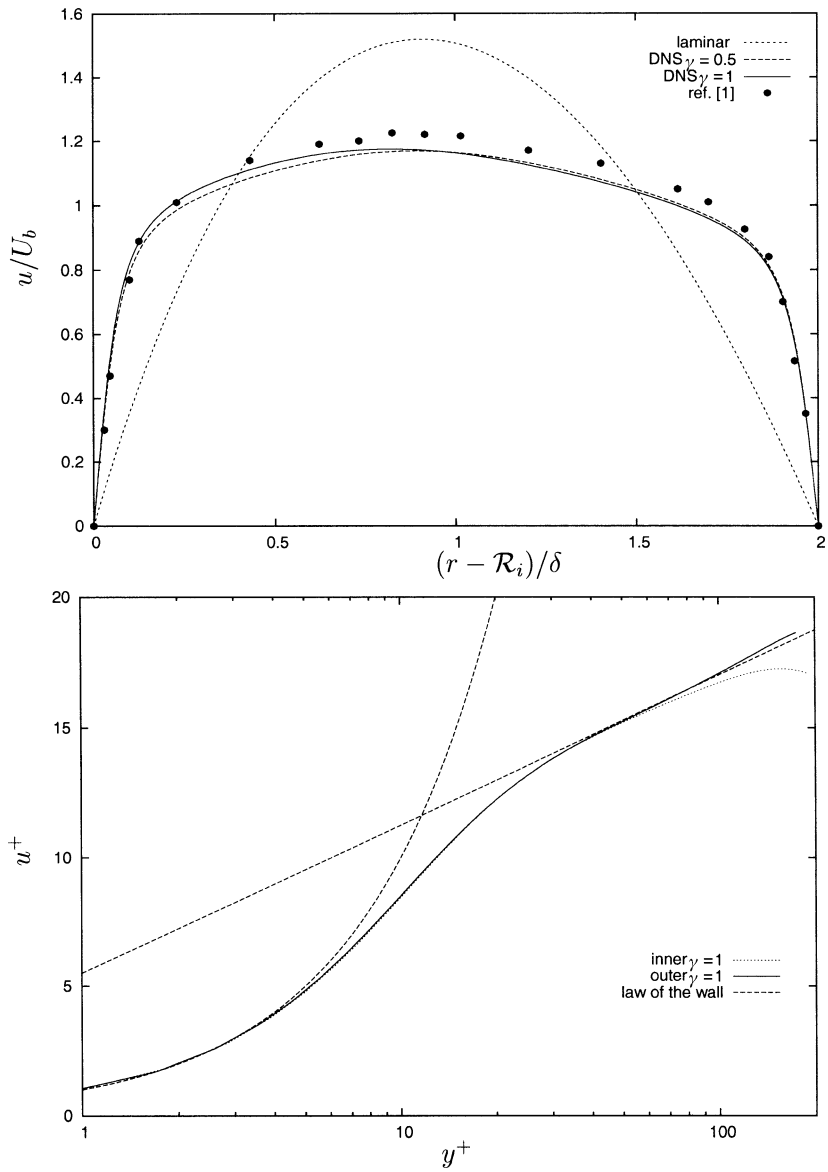

Fig. 2. Top: comparison between the computed turbulent profiles ($\gamma = 0.5$ and $\gamma = 1$) of the longitudinal mean velocity and the analytical laminar profile for $\gamma = 1$. Experimental data from [1], collected at $\gamma = 1$ but at a different Reynolds number, are also shown for comparison. Bottom: longitudinal mean velocity distribution, plotted in viscous units, over the inner (dotted line) and the outer (continuous line) wall, for $\gamma = 1$ only. The two limiting behaviors of the planar case (dashed line) are $u^+ = y^+$ for the viscous sublayer and $u^+ = 2.5 \ln y^+ + 5.5$ for the logarithmic layer. Here and in the following $y^+ = (r - \mathcal{R}_i)^+$ for the inner wall, and $y^+ = (\mathcal{R}_o - r)^+$ for the outer wall.

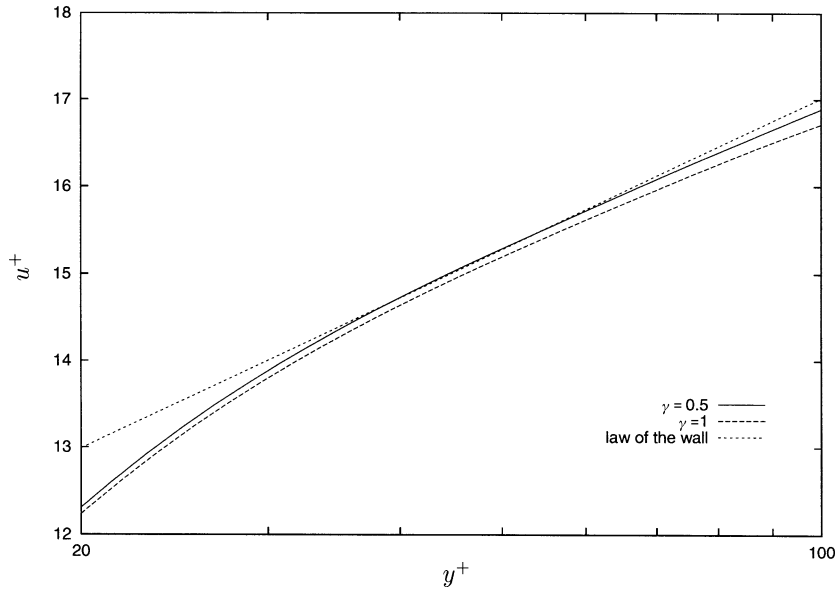

Fig. 3. Longitudinal mean velocity distribution, plotted in viscous units, in the logarithmic region over the inner wall: computed profiles for $\gamma = 0.5$ (dotted line) and $\gamma = 1$ (continuous line). Dashed line is the planar law of the wall $u^+ = 2.5 \ln y^+ + 5.5$.

shifted towards the inner wall at $(r - \mathcal{R}_i)/\delta \sim 0.91$. The turbulent profile is flatter, as it always is, and its asymmetry increases with curvature. When $\gamma = 1$ the maximum of the profile is at $(r - \mathcal{R}_i)/\delta \sim 0.82$. The overall agreement with experimental data available for $\gamma = 1$ from the measurements made by [1], but at the somewhat lower Reynolds number of $\mathrm{Re}_b = 4450$, is adequate, especially in the near-wall portion of the profile. It can be observed that the experimental data are such that its mean value is not exactly unity, and therefore they are not actually scaled with the bulk velocity. Experimental and DNS curves collapse much better if the experimental data are renormalized to unity mean value. To further verify our data, we have conducted an additional simulation with a modified version of the second-order finite-difference computer program described in [14], the source code of which was made available courtesy of P. Orlandi: this simulation has confirmed the present results.

An "inner" look at the mean-velocity profile can be obtained by plotting it in semilog axes and normalizing velocities and lengths with inner variables. This is where the law of the wall classically appears. Our profile is shown in this form in Fig. 2 (bottom), for $\gamma = 1$ only but for both walls, each normalized with the relevant friction velocity. The distance y^+ from the pipe walls is defined as $(r - \mathcal{R}_i)^+$ for the inner wall and $(\mathcal{R}_0 - r)^+$ for the outer wall. The classical log law $u^+ = 2.5 \ln y^+ + 5.5$ is also shown for reference, and can be considered the behavior of the plane channel flow in the logarithmic layer, whereas near the wall it is simply $u^+ = y^+$.

Farther from the wall, at these values of Reynolds number and curvature, the profile over the outer wall presents a relatively well defined logarithmic region, where both the slope and the intercept of the straight line are in agreement with the universal values of the planar case. On the other hand, the inner wall shows this characteristic to a much lesser extent.

The effect of the transverse curvature on the slope of the logarithmic portion of the profile can be evaluated in Fig. 3. Here we report an enlargement of Fig. 2 (bottom), centered in the logarithmic portion, showing the profiles for both $\gamma = 0.5$ and $\gamma = 1$ for the inner wall only. It can be seen that, in the case with less curvature, the mean velocity profile over the inner wall still follows very closely the universal behavior of the plane case, while an increase of curvature causes a downward shift of the profile compared to the plane channel flow. There is at least a visual indication that the slope of the profile may change, but a more extensive analysis over a wider range of radius ratios is needed to support this conclusion.

For the inner wall these results are in general qualitative agreement with the DNS study in [2], where, however, much higher curvatures were considered. Here the use of a fraction of a turn as the base period for the azimuthal discretization enabled us for the first time to explore mild curvatures and the smooth transition to a plane-channel behavior. Both Neves et al. [2] and we found that, in agreement with many experimental observations conducted in turbulent boundary layers over small cylinders, the slope of the mean velocity profile in the logarithmic region decreases with transverse curvature. However, in the high-curvature regime there is still no agreement between experiments and the numerical simulations of [2] concerning the quantification of this effect.

In addition, while it is reasonable that, in the limit of vanishing curvature, a universal behavior of the mean velocity profile in the logarithmic region should be smoothly approached, there is no indication in the literature regarding the law with which

transverse-curvature effects begin to affect the logarithmic layer. The present study has shown that a relatively low value of $\gamma = 1$ with $\mathcal{R}_i^+ \sim 190$ is enough for the log layer to be appreciably affected.

6. Turbulence statistics

Fig. 4 (top) shows the root-mean-square values of the turbulent velocity fluctuations for the case with $\gamma = 1$ only, and for comparison provides the analogous quantities computed in the plane channel flow by [8], at a similar Reynolds number of $\mathrm{Re}_\tau = 180$. In analogy with the mean velocity profile, the r.m.s. profiles of all three velocity components in the annular pipe exhibit an evident asymmetry. The asymmetry is more pronounced in the central part of the gap. The peak values of the root-mean-square velocity components are also somewhat different at the inner and outer wall: the peak of the axial component is

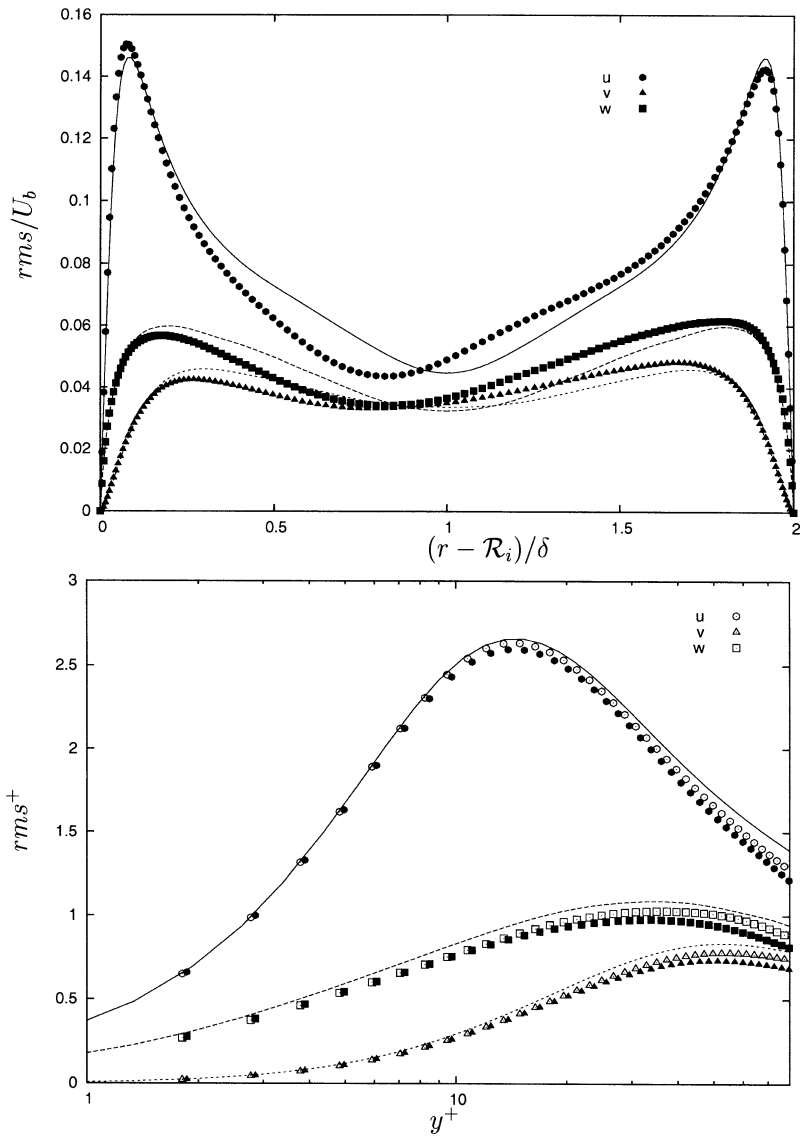

Fig. 4. Top: root-mean-square values of velocity fluctuations for $\gamma = 1$ (filled symbols), plotted in outer units, compared with the plane channel flow (lines). Channel data from [8] at the same Reynolds number. Bottom: root-mean-square values of velocity fluctuations over the inner wall for $\gamma = 0.5$ (open symbols) and $\gamma = 1$ (filled symbols), plotted in inner units, compared with the plane channel flow data (lines) from [8].

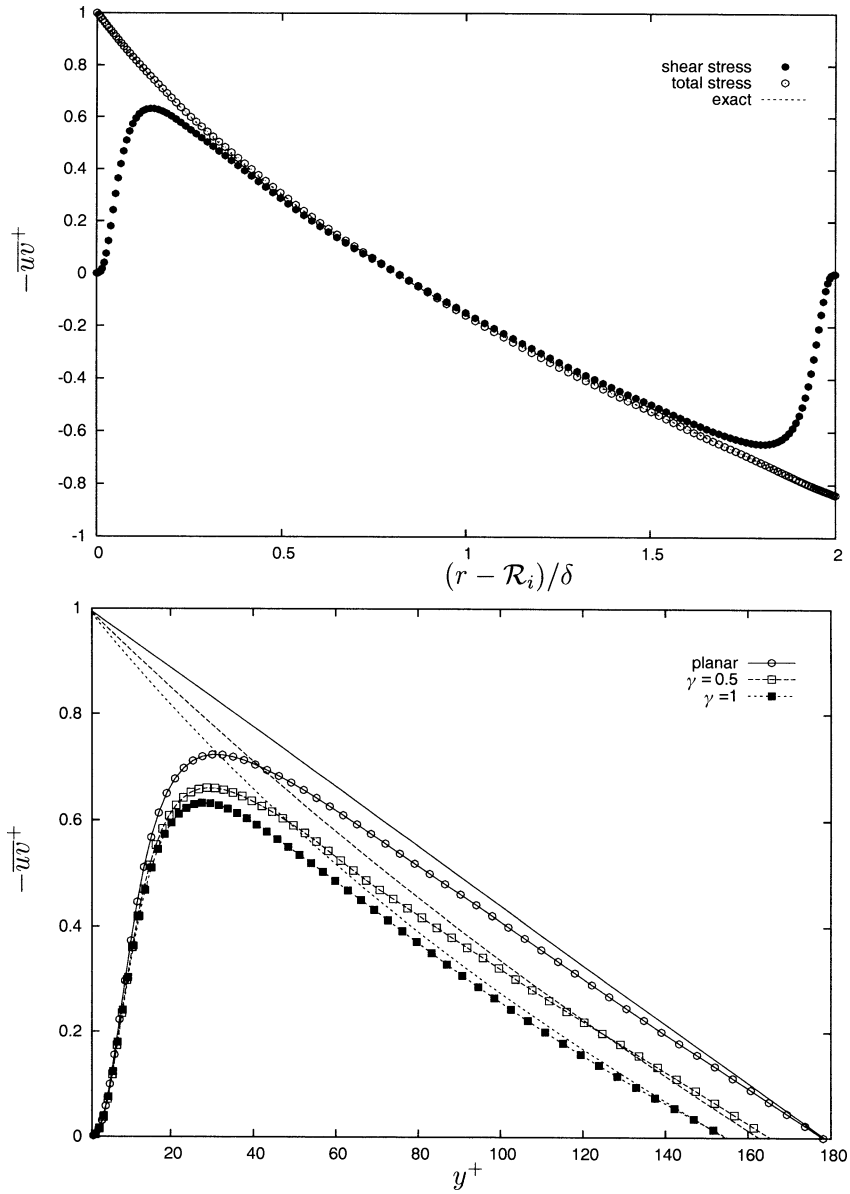

Fig. 5. Top: Reynolds stresses component $-\overline{uv}^+$ (filled symbols) and total shear stress $-\overline{uv}^+ + 1/\mathrm{Re}_\tau \; \mathrm{d}U^+/\mathrm{d}r^+$ (open symbols) for $\gamma = 1$, plotted versus $(r - \mathcal{R}_i)/\delta$. Dotted line correspons to the analytical expression of the total stress. Bottom: Reynolds stresses component $-\overline{uv}^+$ for $\gamma = 0.5$ (open squares) and $\gamma = 1$ (filled squares), plotted versus y^+ and compared to total stresses. Plane channel data (open circles) from [8].

slightly increased over the inner wall and correspondingly decreased over the outer wall, while the opposite is true for the other two components.

The same quantities are plotted in Fig. 4 (bottom) in inner units, for both γ's and the inner wall only, again together with plane-channel data from [8]. In these units a general decrease of the fluctuations with curvature can be appreciated, even in the case with smaller curvature. The axial component is the less affected by curvature, while the azimuthal and radial components are more sensitive and show a likewise reduction.

These results extend to low curvature the findings of [2] over a cylinder of much smaller radius, and are consistent with many experiments performed in the high-curvature range.

Fig. 5 (top) shows the plot, in the radial direction, of the Reynolds shear stress $-\overline{uv}/u_\tau^2$ and the total shear stress $-\overline{uv}/u_\tau^2 + 1/\mathrm{Re}_\tau \; \mathrm{d}U^+/\mathrm{d}r^+$ for the case with higher curvature. The mean total stress must balance the applied axial pressure

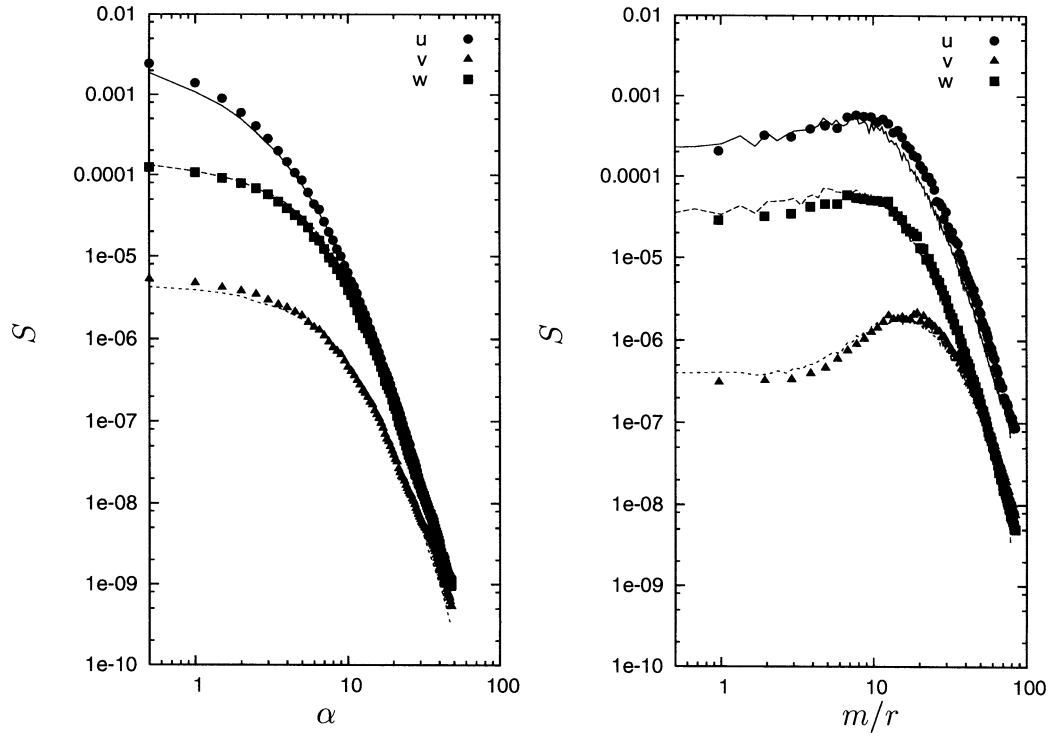

Fig. 6. Streamwise (left) and azimuthal (right) one-dimensional power spectral density functions of fluctuating velocity components, for $\gamma = 1$ at a distance of $y^+ \sim 5$ from the inner (symbols) and the outer (lines) walls.

gradient, and can therefore be calculated *a priori* and exactly. Unlike the plane case, the total stress is not a linear function of the normal coordinate anymore, but its profile is made asymmetric by the curvature. The theoretical total stress profile is also reported in the figure, and is nearly indistinguishable from the DNS data, indicating that a statistically steady state has been attained.

The peak of the Reynolds stress is reduced as a consequence of curvature when compared to the planar case, as already reported by [2] for higher curvatures. This reduction is also evident in the mild-curvature range investigated here. Fig. 5 (bottom) shows that the peak values near the inner wall are smaller than the planar value, and that the effect is roughly proportional to the curvature. The radial position of the peak value also tends to move closer to the wall as the curvature increases. However, it is also evident that this effect is essentially due to the different shape and slope of the total-stress curve, whereas the wall layer is not visibly affected.

The one-dimensional power spectral density distributions of the velocity components are shown in Fig. 6, as functions of the axial and azimuthal wavenumber, for $\gamma = 1$ and a distance of $y^+ \sim 5$ from the inner and outer walls. The spectra in the axial direction (left) confirm the adequacy of the spatial resolution of the present simulations, already discussed in Section 4 and comparable or better than typically used in plane-channel flows. The axial spectra show almost seven decades of energy decrease between the low- and high-wavenumber regions. By considering the spectra in the azimuthal direction (right), one can notice that, despite the azimuthal extension of the computational domain (lowest wavenumber) in the neighborhood of the outer wall is twice that of the inner wall, the use of variable-number-of-modes Fourier series, truncated depending on radius, has allowed us to maintain a fair and constant resolution throughout the whole annular gap.

The autocorrelation in the streamwise direction of each of the three velocity components is displayed in Fig. 7 (left), where data pertaining to the inner and outer wall are compared. The autocorrelation of the axial component can be observed to fall to zero at a separation less than half the length of the computational domain, an indication that the length is sufficient for the periodic boundary conditions to be adequate. The other two velocity autocorrelations, characterized by a shorter length scale and hence only plotted for a limited range of axial separations, reveal that near the inner wall the correlation lengths are greater than near the outer wall, thus suggesting the presence of more elongated turbulence structures near the inner wall. The azimuthal autocorrelation functions are reported in Fig. 7 (right). $(r\Delta\theta)^+$ is the distance in wall coordinates along the circumference. There can be seen that all the transversal length scales tend to be reduced over the inner wall. This is more apparent for the axial and transversal velocity components, whereas the autocorrelation of the radial component exhibits a more pronounced

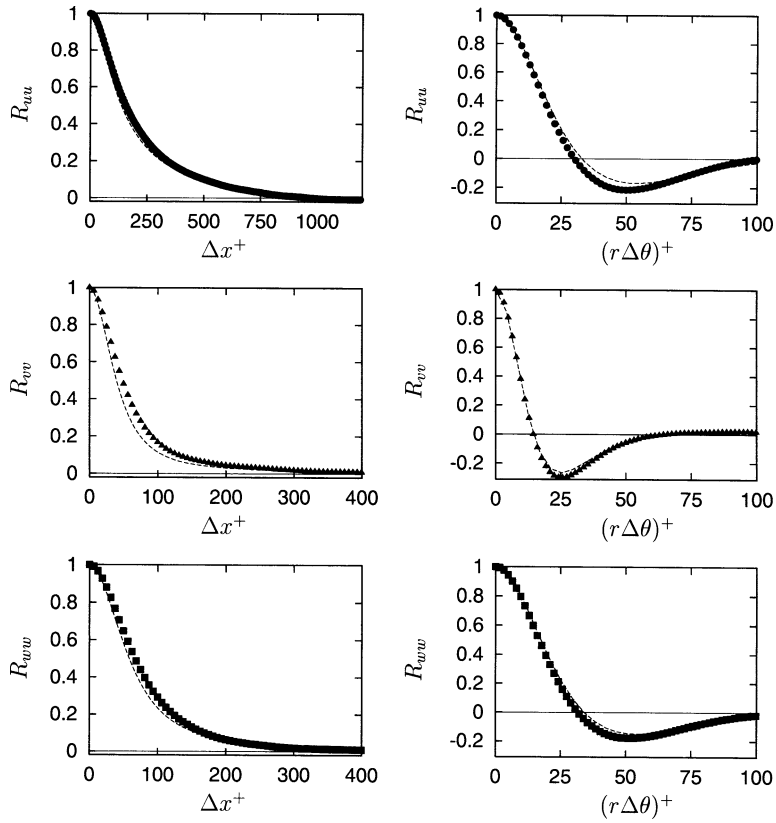

Fig. 7. Left: autocorrelation functions for the fluctuating velocity components versus the streamwise separation Δx^+, for $\gamma = 1$, at a distance of $y^+ \sim 5$ from the walls. Comparison between the inner (symbols) and the outer (continuous line) walls. Note the different axis scale for the streamwise separation in the upper left figure (axial component). Right: autocorrelation functions for the fluctuating velocity components as a function of $(r\Delta\theta)^+$, for $\gamma = 1$ only, at a distance of $y^+ \sim 5$ from the walls. Comparison between the inner (symbols) and the outer (continuous line) walls.

minimum located at approximately the same transversal separation. These results are consistent with the observation, made by [2], that the average spacing between the low-speed streaks which populate the inner layer is reduced as a consequence of the transverse curvature. The same effect can be measured here, to a lesser extent, even if the curvature is much smaller than considered in that paper.

7. Conclusions

The numerical formulation of the Navier–Stokes equations in cylindrical coordinates presented in this paper has allowed us to solve them with a high computational efficiency, employing numerical techniques already well tested in the cartesian geometry and writing a computer code which shares its essential structure with its cartesian counterpart. We have successfully simulated for the first time the turbulent flow in an annular pipe with relatively low transverse curvature. For this purpose a very demanding DNS with more than 16 million unknowns has been performed on a single dual-processor commodity Personal Computer, with very moderate memory requirements and an overall computing time of the order of 15 days.

The problem of the nonuniform azimuthal resolution, which depends on r in cylindrical coordinates, has been overcome by adopting a representation of the flow variables with finite Fourier series whose number of modes depends on the radial coordinate itself. This procedure, which is very general in itself and might be applied in the future to all simulations involving the cylindrical coordinate system, has both contributed a reduction in computational requirements and alleviated potential stability problems. Moreover, the use of a fraction of a turn as the base period for the azimuthal discretization enabled us for the first time to explore very mild curvatures and the smooth transition to a plane-channel behavior.

Results, in terms of mean flow properties and main turbulence statistics, have been presented for the turbulent flow in an annular pipe with two different values of curvature, both in the low range where the common belief was that the flow should

behave essentially as a planar flow. This is not the case, as even mean quantities like the friction velocity exhibit an appreciable deviation from their planar value. The total friction, that is the pressure gradient required for a given flow rate, turns out however to be essentially unchanged. Effects of the azimuthal curvature are also visible in the mean velocity profile plotted in logarithmic coordinates (law of the wall), but mostly at the inner wall whereas the outer-wall profile is almost coincident with the universal law of the planar case. The effects of transverse curvature on the root-mean-square velocity fluctuations are of smaller entity, but in the same qualitative direction as in a related study by [2] concerning a range of much higher curvatures. The peaks of the Reynolds stress are significantly modified by the transverse curvature of the wall, but in a way that can be simply ascribed to the modification of the total stress.

Acknowledgements

Ing. Patrick Morandi is thanked for his work on some of the computations. The financial support of the Italian Space Agency and of the Italian Ministry of University and Research is acknowledged. Part of this work was orally presented at the 4th EUROMECH Fluid Mechanics Conference, Eindhoven, November 2000.

References

[1] J. Nouri, H. Umur, J. Whitelaw, Flow of Newtonian and non-Newtonian concentric and eccentric annuli, Journal of Fluid Mechanics 253 (1993) 617–641.
[2] J.C. Neves, P. Moin, R.D. Moser, Effects of convex transverse curvature on wall-bounded turbulence. Part 1. The velocity and vorticity, Journal of Fluid Mechanics 272 (1994) 349–381.
[3] R.M. Lueptow, P. Leehey, T. Stellinger, The thick, turbulent boundary layer on a cylinder: Mean and fluctuating velocities, Physics of Fluids 28 (12) (1985) 3495–3505.
[4] G. Rao, Law of the wall in a thick axisymmetric boundary layer, Journal of Applied Mechanics 34 (1967) 237.
[5] W. Willmarth, R. Winkel, L. Sharma, T. Sogar, Axially symmetric turbulent boundary layers on cylinders: Mean velocity profiles and wall pressure fluctuations, Journal of Fluid Mechanics 76 (1976) 35–64.
[6] S. Satake, H. Kawamura, Large Eddy simulation of turbulent flow in concentric annuli with a thin inner rod, in: F. Durst, N. Kasagi, B. Launder, F. Schmidt, K. Suzuki, J. Whitelaw (Eds.), Turbulent Shear Flows, Vol. 9, Springer-Verlag, 1995.
[7] I. Shapiro, L. Shtilman, A. Tumin, On stability of flow in an annular channel, Physics of Fluids 11 (10) (1999) 2984–2992.
[8] J. Kim, P. Moin, R. Moser, Turbulence statistics in fully developed channel flow at low Reynolds number, Journal of Fluid Mechanics 177 (1987) 133–166.
[9] P. Orlandi, M. Fatica, Direct simulations of turbulent flow in a pipe rotating about its axis, Journal of Fluid Mechanics 343 (1997) 43–72.
[10] B. Ma, Z. Zhang, F. Nieuwstadt, C. van Doorne, On the spatial evolution of a wall-imposed periodic disturbance in pipe Poiseuille flow at $Re = 3000$. Part 1. Subcritical disturbance, Journal of Fluid Mechanics 398 (1999) 181–224.
[11] M. Manna, A. Vacca, An efficient method for the solution of the incompressible Navier–Stokes equations in cylindrical geometries, Journal of Computational Physics 151 (1999) 563–584.
[12] M. Quadrio, P. Luchini, A 4th order accurate, parallel numerical method for the direct simulation of turbulence in cartesian and cylindrical geometries, in: Proc. of the XV AIMETA Congress on Theoretical and Applied Mechanics, 2001.
[13] M. Rai, P. Moin, Direct simulations of turbulent flow using finite-difference schemes, Journal of Computational Physics 96 (1991) 15.
[14] R. Verzicco, P. Orlandi, A finite-difference scheme for three-dimensional incompressible flows in cylindrical coordinates, Journal of Computational Physics 123 (1996) 402–414.